

2016-11

Crack path and fracture analysis in FSW of small diameter 6082-T6 aluminium tubes under tension-torsion loading

Maggiolini, E

<http://hdl.handle.net/10026.1/5132>

10.1016/j.ijfatigue.2016.02.043

INTERNATIONAL JOURNAL OF FATIGUE

Elsevier BV

All content in PEARL is protected by copyright law. Author manuscripts are made available in accordance with publisher policies. Please cite only the published version using the details provided on the item record or document. In the absence of an open licence (e.g. Creative Commons), permissions for further reuse of content should be sought from the publisher or author.

Crack path and fracture analysis in FSW of small diameter 6082 aluminium tubes under tension-torsion loading

E Maggiolini ¹, R Tovo ¹, L Susmel ², M N James ^{3,4} and D G Hattingh ⁴

Abstract

This paper reports part of the work done in a research project aimed at developing an optimised process to join 38 mm diameter tubes of 6082-T6 aluminium alloy using friction stir welding (FSW), and then to determine the fatigue performance under tension, torsion and tension-torsion loading conditions. The final outcome of the project is intended to be guidance for fatigue design of small diameter aluminium tubes joined by FSW, and this paper presents information on crack path and defects under the various loading conditions. Crack path analysis was performed using both low magnification stereo microscopy and scanning electron microscopy, in order to identify crack initiation sites, the direction of crack propagation and the interrelated influence of microstructure and weld geometry on the crack initiation path.

Keywords

Friction stir welding; multiaxial fatigue; tension-torsion; 6082-T6 aluminium; small diameter tube; crack path.

Introduction

Welding is the most common joining process in structural design and general manufacturing, and is statistically reliable provided that joint design adheres to codified guidelines. Nonetheless, cracking problems are often observed to be associated with the weld zone, arising from microstructural changes due to the weld thermal cycle, residual stresses induced by differential heating and cooling, and defects introduced in the weld zone either by local geometry changes (stress concentration points) or from the welding process (particularly in fusion welding, which is

¹ Department of Engineering, University of Ferrara, Ferrara, Italy

² Department of Civil & Structural Engineering, University of Sheffield, Sheffield, England

³ School of Marine Science & Engineering, University of Plymouth, Plymouth, England

⁴ Department of Mechanical Engineering, Nelson Mandela Metropolitan University, Port Elizabeth, South Africa

a casting process). Hence a major challenge faced in fatigue design is that of determining an optimum welding process and parameters that leads to efficient and reliable joints. However, when deploying newer solid-state friction stir welding processes to innovative applications, e.g. joining of small diameter tubes such as might be used in structural design for ground vehicles, there are currently no agreed guidelines that can be applied to fatigue design. The overall objective in this research project was therefore the identification of suitable fatigue design techniques for small diameter friction stir welded (FSW) tubular structures. This paper reports that part of the project that was aimed at characterising crack initiation sites and the subsequent crack path.

Friction stir welding is a solid-state process that was developed at TWI in Cambridge [1]) and it offers high quality welds [2], low residual stresses transverse to the weld joint [3], [4], high fatigue strength [5], a fine grained weld nugget compared with other welding techniques [6], along with minimal joint preparation and a low requirement for post-weld dressing. Disadvantages of the FSW technique include the keyhole left after tool withdrawal, the requirement for a large downwards forging force and rigid clamping along with a lower weld traverse rate than some fusion welding techniques (although FSW rates of 2 m/min have been reported [7]). FSW has therefore been deployed across many areas of manufacturing, including the space industry [7], ships [8], aircraft [9] and ground transportation [10].

Whilst it is easy to join flat plate with FSW, it can be difficult to extend its applications to include tubes, in particular small diameter tubes, and other complex geometries. Friction stir welding of tubes has particular challenges in terms of pin plunge depth and support for the material during welding and also in terms of arranging tool pin retraction as a weld is completed, in a manner that does not to leave the typical plunge hole in the joint line. A friction stir welding process was specifically developed for this project at Nelson Mandela Metropolitan University in South Africa to join extruded 6082-T6 aluminium alloy tubes with an approximate outer diameter (OD) of 38 mm and a wall thickness of approximately 3.5 mm (giving an inner diameter (ID) of some 31 mm).

An MTS I-STIR™ Process Development System provided the foundation for this work, which involved coupling a worm gear motor with a tube support system for the welding process, and integrating the drive system control with that of the I-STIR platform (see Figure 1). As noted above, it is important in FSW of small diameter tubes, where provision for run-on and run-off tabs cannot be provided, not to leave any hole in the joint line after extracting the tool at the end of the welding process; the resulting hole in the joint would act as a very significant weld defect, given the relative sizes of the tool pin, tube diameter and tube wall thickness. A tool with a self-retracting pin was therefore also designed and developed for this particular FSW application.

This is one of very first applications of FSW to small diameter tubular geometries to be reported in the open literature. Peterson et al [11] filed a US patent application in 2011 for a process to friction stir weld casing and small diameter tubing or pipe, although they defined ‘small’ diameter as an ID \approx 228 mm. Lammlein et al [12] have published work dealing with the development of a process for FSW of 6061-T6 aluminium tubes 107 mm in diameter and with a wall thickness of approximately 5.8 mm. Both of these cases deal with substantially larger diameters than the 38 mm tube used in the present work and this smaller size was chosen to be representative of the dimensions that might be used in space frame chassis design for ground vehicles. Chen et al [13] have also published work on the development of a FSW process for joining 19 mm diameter pipes of 3003 aluminium alloy to pure copper with a 1 mm wall thickness. They made the welds on an adapted lathe and performed tensile tests but did not consider fatigue data.

In contrast, a wealth of data is available for FSW in plates and weld performance has been well characterised in terms of process optimisation and residual stresses [14], static and dynamic mechanical properties [15-16], the influence of weld tool travel speed [17] and weld thermal modelling [18-19].

The welding process

A number of individual tasks had to be accomplished with respect to process development, before the tube specimens required for the multiaxial fatigue testing could be manufactured in the

number required for the test programme (circa 100) with confidence that their properties would be sufficiently consistent to provide reliable fatigue data. These major tasks included:

- a) To design and build the worm gear drive and clamping system for welding;
- b) Electronic integration of this drive into the control software of the I-STIR process development system;
- c) Design and validation of the retracting pin tool used in the welding process;
- d) Determination of suitable welding process parameters to achieve the required weld quality;
- e) Production of 200 mm long welded test specimens for initial microstructural and mechanical property characterisation of the joint.

Figure 2 shows details of the clamping system and the various components are identified as given below:

- 1. Precision locknut
- 2. Fenlock cone clamp
- 3. Flange connecting motor to tube drive shaft
- 4. Support bearings
- 5. Tube to shaft coupling
- 6. Motor keyway lock bolt

The process of aligning the tubes and clamping them in position for welding is quite time-consuming and any extension of this process into industry would require an increased level of automation to be introduced into the process compared with this prototype process. Key issues in the clamping operation include achieving accurate alignment which is fundamental to achieving a high quality weld; heat retention during welding of multiple tube specimens, which makes it increasingly difficult to release the cone clamps (probably because of expansion of the threads

on the release bolts which necessitated replacement of a number of these bolts during the production run of 100 specimens); difficulty in achieving an even clamping force on the tubes caused by differences in ID of the tubes and by different out-of-round measurements both of which lead to distortion of the tube during setup. The sequence of events during welding is outlined in Figure 3 and it should be noted that it was found necessary to machine the tube OD to 37.5 mm to improve the tube alignment during set-up.

The weld process used force control on a small diameter tool shoulder of 10 mm rotating at 600 rpm, an optimised rotational tube feed rate of 50 mm/min, and a tool pitch angle of 2°. It was found necessary to weld the tube through a rotation of 720°, i.e. two complete revolutions, in order to achieve a good surface finish; the first pass improves the uniformity of shoulder contact and hence the second pass improves the surface finish. In optimising the tool geometry, the pin penetration depth was initially set to approximately 85% of the nominal tube wall thickness and the quality of the resulting weld was evaluated via metallographic examination after welding. A pin length of 2.45 mm was found to work very effectively with a plunge depth of 2.5 mm to ensure adequate shoulder contact. Figure 4 and the associated information on weld process parameters in Table 1 demonstrate the influence of the tool rotational feed rate, tool rotational speed and number of complete revolutions of the tube on the quality of weld surface finish, which is a key controlling factor in fatigue performance. Full details of the development and optimisation of the welding process will be reported elsewhere.

One hundred fatigue specimens were manufactured by joining two 110 mm lengths of 6082-T6 aluminium tube with friction stir welding, as shown in Figure 5. The chemical composition of this alloy is given in Table 2. Once the samples had been manufactured in South Africa, they were sent to the University of Sheffield and the University of Ferrara for the mechanical testing part of the programme. Tensile fatigue testing was carried out in Ferrara with a load ratios of $R = 0.1$ and $R = -1$, while torsion fatigue and biaxial tension-torsion testing were carried out in Sheffield with load ratios of $R = 0$ and $R = -1$. The tensile fatigue testing used a 250kN MTS servohydraulic fatigue testing machine and a Schenk servohydraulic tension-torsion fatigue testing machine was

used for the tension-torsion work. Biaxial fatigue testing used both in-phase (IPh) and out-of-phase (OPh) constant amplitude sinusoidal loading. Table 3 gives the relevant data on the testing programme where the biaxiality stress ratio $\lambda = \frac{\sigma_a}{\tau_a}$, with σ_a being the tensile stress amplitude and τ_a is the torsional stress amplitude in the fatigue cycling, while Θ is the phase angle between tension and torsion loading.

After testing, the fractured specimens were sent to the University of Plymouth for fractographic and metallographic analysis of the fracture surfaces and crack paths. This part of the work entailed acquiring data from light and scanning electron microscopy, polarised light metallography and electron backscatter diffraction of specific crack initiation regions. The aim was to develop a compendium of fractographs and crack initiation sites, along with relevant microstructural information, as underpinning information for the fatigue life prediction and improvement aspects of the project.

Monotonic mechanical properties

The tensile properties of a welded joint are a reasonable first order indicator of the joint quality and 'joint efficiency' (defined as the ratio of tensile strength of the weld to that of the parent plate) is often used to describe the mechanical performance of welded joints. In the present case the tensile strength was measured on complete tubes and on microtensile specimens. Tests on the microtensile specimens, with a cross-section of 2 mm by 3 mm (Figure 6) were intended as trials of the viability of using a Gatan Microtest 2000EW test module in a scanning electron microscope (SEM) whilst performing microstructural characterisation under load via electron backscatter diffraction (EBSD). Very consistent tensile strength values were recorded from both types of tensile test, and mechanical property data in tension and in torsion are shown in Table 4. The welded joint efficiency is 0.55; this value compares well with the figure of 0.67 reported for FS welds in 3 mm thick plates of 6082-T6 [15]. The microtensile specimens were polished in order to observe where failure occurred and this was found to be in the weld zone on the tool retreating

side. The tube specimens failed at the tool shoulder undercut on either the advancing or retreating sides of the weld, which represents a stress concentrating feature.

Fatigue crack path analysis

Once the fatigue tests had been completed the tube specimens were pulled apart to reveal the fracture surfaces and an analysis of the crack initiation site and crack path was performed on each specimen. This entailed identifying and recording the test conditions for each specimen, determining whether the crack lay on the advancing or retreating side of the weld, or was in the weld itself, the circumferential position at which the crack had initiated relative to the stop-start position for those specimens where this was possible, recording the fractographic appearance of the crack using both low magnification light microscopy and scanning electron microscopy and, in certain cases, using optical metallography or electron backscatter diffraction to follow the crack path through the microstructure at the initiation site.

To assist in this fractographic analysis, crack initiation sites were defined in terms of their angular position relative to the stop-start position in the weld, given as 0° in Figure 7 where the advancing side of the weld is towards the top in the figure, and the retreating side is towards the bottom. The procedure adopted in documenting the crack path and defects was to record the entire fracture surface using digital images and then to identify crack initiation points and any other interesting features for closer inspection using scanning electron microscopy. Crack initiation was primarily closely associated with the slight undercut at the edge of the weld zone arising from the tool shoulder, but could occur on either the advancing or retreating side of the weld, which exhibit individual variations in values of hardness and residual stress. Table 5 gives the location of crack initiation for all the specimens tested in tensile fatigue. In the two specimens that were left intact (W117: 709,775 cycles and W121: 476,829 cycles) cracking had initiated along the middle plane of the weld zone and one specimen fractured through the middle of the weld (W118: 1,247,627 cycles). As is usually the case with welded specimens, the fatigue life can be quite variable at specific values of applied stress range and this reflects the presence on the weld surface of tool marks (arising from the tool advance in each tool revolution), the tool shoulder undercut and any

near-surface defects. In the majority of the specimens (58%) cracking initiated at the advancing side of the weld, at the retreating side in 27% of the specimens and in other locations in 15% of specimens. It is likely that the slight increase often observed on the advancing side of the weld in the value of tensile residual stress in the direction transverse to a friction stir weld [4] underlies this predilection for crack initiation on the advancing side under a tensile load.

Table 6 presents the data for the torsional specimens, and it should be noted that the torsional loading damages the fracture surfaces and usually makes impossible post-hoc determination of the crack initiation point around the circumference. The torsional data indicates a significant influence of both stress ratio R and shear stress amplitude on the position and crack path associated with crack initiation. Thus under torsional fatigue loading with $R = 0$, crack initiation occurred on the retreating side in all welds examined, whilst under reversed loading with $R = -1$ crack initiation predominantly occurs on the advancing side. Under torsional loading, at the two lowest shear stress ranges used in both $R = 0$ and $R = -1$ loading, the crack path does not follow the undercut zone at the sides of the weld, but instead shows a more classical shear crack initiation at an angle of approximately 45° (see the two images given in Figure 8).

The fatigue data and information on initiation location is given in Table 7 for the in-phase and out-of-phase tension-torsion testing. It is clear that cracks can initiate with approximately equal facility on either the advancing or retreating side of the weld which implies that the local multiaxial strain state is more important than the effects of hardness changes or residual stress induced in the friction stir welding process. An interesting observation is that in a number of tests the crack moved from the advancing to the retreating side during growth although this does not seem to have any relationship with load parameters (Figure 9). In the case of the torsion specimens, multiple crack initiation sites along the retreating side of the weld were observed under $R = 0$ loading across the range of applied stress values, e.g. T23 (92 MPa), T16 (67 MPa). Figures 10 and 11 show examples of such multiple initiation sites. It can also be observed that the number of cracks initiated appears to increase as the applied shear stress decreases and hence the

fatigue life increases. A problem with those specimens that displayed multiple crack initiation but that did not completely fracture, was that the primary initiation site could not be determined because of the difficulty in separating the specimen at the appropriate place, e.g. Figure 11.

Certain of the in-phase tension-torsion specimens, e.g. IPh8 and the torsion specimens, e.g. T4 exhibited crack initiation coincident with the stop-start position, as shown in Figures 12 and 8a, respectively. Torsion fatigue specimens occasionally showed classic shear crack bifurcation under torsion loading with $R = -1$ and Figure 13 shows an example of this type of cracking where crack initiation has also occurred at the stop-start position. Table 8 summarises the crack location information for all specimens and shows that for the 62 specimens where this information was obtained, 50% of cracks initiated at the advancing side, 39% at the retreating side and 11% at other positions in the weld.

In specimens that had not experienced significant surface damage during torsion or reversed tension loading, it was generally straightforward to locate the primary crack initiation site, although where multiple cracks of similar size had occurred the fracture surfaces could not be easily exposed. Crack initiation generally occurred at the surface undercut caused by the tool shoulder at either advancing or retreating sides of the weld, and this is demonstrated in Figure 14 (tensile fatigue specimen W121) where ratchet marks are present on the fracture surface that correspond with the tool shoulder marks, and a small fatigue crack has initiated between these marks (indicated with an arrow). Occasional wormhole defects, which are a relatively common form of FSW defect, were observed on the fracture surface (see the tensile fatigue specimen W117 shown in Figure 15). The mechanism by which such defects are formed reflects the details of the plastic mixing process during friction stir welding and has been described in reference [20] which also summarises other forms of FSW defect.

The specimens tested under biaxial tension-torsion loading were more interesting, as although parts of the fracture surfaces had suffered damage from contact during crack growth, certain

specimens indicated that although the primary crack had initiated at the outside of the tube (in-phase tension-torsion specimen IPh2 - Figure 16), smaller secondary cracks had sometimes formed at the inner surface later in the fatigue process (IPh2 - Figure 17). Figure 17 also demonstrates that the formation of this secondary crack occurred at a late stage in the fatigue process because the fracture surface fairly quickly starts to reflect the underlying 'onionskin' structure in the weld zone, reflecting high levels of applied load and hence high growth rates. Where fracture surfaces were undamaged, the mechanism of fatigue crack growth could be observed to be ductile striation formation as shown in Figure 18 (tension fatigue specimen W130).

Metallography

Ultimately, it is intended to evaluate the microstructure and crack path using polarised light microscopy and electron back-scatter diffraction (EBSD) in a scanning electron microscope, but this work has not yet been completed. Figure 19 shows a polarised light metallographic montage that shows the complete weld zone for the torsion specimen T6. Individual regions of the microstructure can be examined at higher magnification (Figure 21). This can also be done for cracked specimens, although it entails polishing back the surface to provide a flat region for etching, and the etching process trends to attack crack edges preferentially. This is where EBSD has a distinct advantage over light microscopy, although it also requires a flat surface in order to adequately index the microstructure and the plastic deformation that surrounds cracks can therefore lead to a loss of resolution. Figure 21 shows a typical EBSD image of the crack tip region in specimen T6 at 2,000x magnification and a fairly good resolution of the microstructure has been obtained to within a distance of about 10 μm from the crack edge. The interesting point that this image does not make clear is whether grain refinement has occurred due to plastic strain in the zone near to the crack tip, or whether this apparent effect merely reflects a loss of data in this heavily deformed region. The EBSD image shown in Figure 22 contains the crack initiation region in specimen IPh-1, looking at the crack growing down through the tube thickness. The crack has initiated and grown along the tool shoulder undercut on the advancing side of the weld

and the grain structure reflects the heat-affected zone (HAZ) on the parent plate side of the crack. The direction of crack growth through the tube thickness is shown by the arrows in the top image.

Conclusions

The work described in this paper has summarised some of the crack path observations made during a major three-year research project that has had four international partners working in synergy on developing both a new FSW process for joining small diameter tubes and on characterising the fatigue performance of the tubes under tension, torsion and biaxial tension-torsion loading. In this project the first year was spent developing the FSW technology to successfully join small diameter tubes and optimising the process conditions to achieve consistent mechanical properties (Nelson Mandela Metropolitan University). The next 18 months entailed a complementary programme of fatigue testing at Universities in two countries (Universities of Sheffield and Ferrara), with the fatigued specimens finally being delivered to the University of Plymouth in the last 6 months of the project for fractographic and metallographic characterisation.

It can be concluded that:

1. Small diameter tubes can be successfully welded and can deliver similar values of joint efficiency (0.55) to those observed with flat plates joined by FSW. The main problems arise from designing a process with a retractable tool, obtaining an optimised process, alignment of out-of-round tubes with small wall thickness and heating of the clamping arrangement during a production run.
2. The welding process would need to be automated in order to be taken out into industry, but the pilot project has indicated considerable potential for deployment in the ground vehicle industry.
3. The loading conditions do not affect the location of crack initiation in any significant way in terms of fatigue design, although small variations were observed in, for example, tensile fatigue at stress ratios of either 0.1 or -1. Variations were limited to a move from advancing to retreating side of the weld with crack initiation still generally confined to the undercut groove that occurs at the edge of the tool shoulder.

Acknowledgment

Support for this work from the Leverhulme Trust through the award of International Network Grant IN-2012-107 is gratefully acknowledged.

References

- [1] Thomas W.M., Nicholas E.D., Needham J.C., Murch M.G., Temple-Smith P., Dawes C.J.: "Friction welding.", (1991), PCT/GB92/02203.
- [2] Hussein, S.A., Tahir, A.S.M., Hadzley, A.B.: "Characteristics of aluminum-to-steel joint made by friction stir welding: A review", (2015) *Materials Today Communications*, Vol. 5, pp. 32-49.
- [3] Ji, P., Yang, Z., Zhang, J., Zheng, L., Ji, V., Klosek, V.: "Residual stress distribution and microstructure in the friction stir weld of 7075 aluminum alloy", (2015) *Journal of Materials Science*, Vol. 50, 22, pp. 7262-7270.
- [4] James, M.N., Hughes, D.J., Hattingh, D.G., Bradley, G.R., Mills, G. and Webster, P.J. (2004), "Synchrotron diffraction measurement of residual stresses in friction stir welded 5383-H321 aluminium butt joints and their modification by fatigue cycling", *Fatigue and Fracture of Engineering Materials and Structures*, Vol. 27 pp.187-202.
- [5] Polezhayeva H., Toumpis A.I., Galloway A.M., Molter L., Ahmad B., Fitzpatrick M.E.: "Fatigue performance of friction stir welded marine grade steel", (2015) *International Journal of Fatigue*, Vol. 81, pp. 162-170.
- [6] Krasnowski, K., Hamilton, C. and Dymek, S.: "Influence of tool shape and weld configuration on microstructure and mechanical properties of the AL 6082 alloy FSW joints", (2015) *Archives of Civil and Mechanical Engineering*, Vol. 15 pp. 133-141.
- [7] Shah, S., and Tosunoglu, S.: "Friction stir welding: current state of the art and future prospects", (2012) 16th World Multi-Conference on Systemics, Cybernetics and Informatics, Orlando, FL, July 17-20, 2012.
- [8] Kolligan, K. J.: "Friction stir welding for ship construction", (2004) Article prepared under contract N0014-06-D-0048 for the Office of Naval Research, by Concurrent Technologies Corporation, Harrisburg, PA, 2004.
- [9] Burford, D., Widener, C. and Tweedy, B.: "Advances in friction stir welding for aerospace application", *Airframer*, Issue 14, pp. 3-7, November (2006), Proceedings of the 6th AIAA Aviation Technology, Integration and Operations Conference, Wichita, Kansas, September 25-27, 2006.

- [10] Nicholas, W. M. Thomas and E. D.: "Friction stir welding for the transportation industries", (1997) *Materials and Design*, Vol. 18, Nos. 4/6, pp. 269-273.
- [11] Peterson, J., Hall, J., Steel, R.J., Babb, J., Collier, M. and Packer, S.M. : "Out of position friction stir welding of casing and small diameter tubing or pipe, (2011) Patent Application WO 2011053361 A2, May 2011.
- [12] Lammlein, D.H., Gibson, B.T., DeLapp, D.R., Cox, C., Strauss, A.M. and Cook, G.E.: "Friction stir welding of small diameter pipe: an experimental and numerical proof of concept for automation and manufacturing", (2012) *Proceedings of the Institution of Mechanical Engineers, Part B: Journal of Engineering Manufacture*, Vol. 226 no. 3 pp. 383-398.
- [13] Binxi Chen, Ke Chen, Wei Hao, Zhiyuan Liang, Junshan Yao, Lanting Zhang and Aidang Shan: "Friction stir welding of small-dimension Al3003 and pure Cu pipes, (2015) *Journal of Materials Processing Technology*, 223 pp. 48-57.
- [14] H. Lombard, D.G. Hattingh, A. Steuwer and M.N. James: "Effect of process parameters on the residual stresses in AA 5083-H321 friction stir welds, (2009) *Materials Science and Engineering A* 501 pp. 119-124.
- [15] Moreira, P.M.G.P., Santos, T., Tavares, S.M.O., Richter-Trummer, V., Vilaça, P. and de Castro, P.M.S.T.: "Mechanical and metallurgical characterization of friction stir welding joints of AA6061-T6 with AA6082-T6", (2009), *Materials and Design*, Vol. 30, pp. 180-187.
- [16] Liu, H.J., Fuji, H., Maeda, M., Nogi, K.: "Tensile properties and fracture locations of friction-stir-welded joints of 2017-T351 aluminum alloy", (2003), *Journal of Materials Processing Technology*, Vol. 142, Issue 3, pp. 692–696.
- [17] James, M.N., Hattingh, D.G. and Bradley, G.R.: "Weld tool travel speed effects on fatigue life of friction stir welds in 5083 aluminium", (2003) *International Journal of Fatigue*, 25 pp. 1389-1398.
- [18] Pal, S. and Phaniraj, M.P.: "Determination of heat partition between tool and workpiece during FSW of SS304 using 3D CFD modelling", (2015) *Journal of Materials Processing Technology*, Vol. 222 pp. 280-286.
- [19] Buglioni, L., Tufaro, L.N. and Svoboda, H.G.: "Thermal cycles and residual stresses in FSW of aluminium alloys: experimental measurements and numerical models, (2015) *Procedia Materials Science*, Vol. 9 pp.87-96.
- [20] M.N.James, G.R. Bradley, H. Lombard and D.G. Hattingh: "The relationship between process mechanisms and crack paths in friction stir welded 5083-H321 and 5383-H321 aluminium alloys", *Fatigue and Fracture of Engineering Materials and Structures*, Vol. 28 pp.245-256.

Table 1 Weld process parameters used to make the trial welds shown in Figure 4.

| Weld | Feedrate | Tool rpm | Total rotational angle |
|------|------------|----------|------------------------|
| 1 | 100 mm/min | 600 | 360° |
| 4 | 100 mm/min | 800 | 360° |
| 3 | 100 mm/min | 800 | 720° |
| 2 | 50 mm/min | 800 | 720° |

Table 2 Chemical composition of the 6082 aluminium alloy.

| | Mg | Si | Mn | Fe | Zn | Cu | Ti | Cr | Al |
|----------------------|-----------|-----------|-----------|-----------|-----------|-----------|-----------|-----------|-----------|
| Specification | 0.60-1.20 | 0.70-1.30 | 0.40-1.00 | 0.50 | 0.20 | 0.10 | 0.10 | 0.25 | Balance |
| Tube Alloy | 0.647 | 0.988 | 0.526 | 0.222 | 0.021 | 0.034 | 0.012 | 0.006 | Balance |

Table 3 Summary of the fatigue testing parameters including the biaxiality ratio λ .

| Test | Number of samples | λ | R | Θ° |
|------|-------------------|-----------|-----|----------------|
| A | 10 | ∞ | 0.1 | - |
| B | 9 | ∞ | -1 | - |
| C | 10 | 0 | 0.1 | - |
| D | 14 | 0 | -1 | - |
| E | 7 | 1.73 | 0.1 | 0 |
| F | 7 | 1 | 0.1 | 0 |
| G | 8 | 1.73 | -1 | 0 |
| H | 7 | 1 | -1 | 0 |
| I | 7 | 1.73 | -1 | 90 |
| L | 4 | 1 | 0 | 90 |
| M | 7 | 1.73 | 0 | 90 |

Table 4 Tensile and torsional strength data for the welded 6082-T6 tubes. Superscript 1 indicates microtensile data and superscript 2 relates to complete tube tests.

| | | |
|---------------------------------|---------|---------|
| Parent plate¹ | Tension | 303 MPa |
| Weld zone¹ | Tension | 169 MPa |
| Weld zone² | Tension | 168 MPa |
| Weld zone² | Torsion | 118 MPa |

Table 5 Crack initiation location in the tensile fatigue specimens, defined in terms of their angle from the stop-start position and the position in the weld zone.

| Load ratio | Specimen | $\Delta\sigma$ (MPa) | Cyclic Life | Crack initiation | α° |
|----------------|----------|----------------------|-------------|------------------|----------------|
| R = 0.1 | W119 | 154.4 | 17,200 | Advancing side | -135 |
| | W111 | 154.4 | 19,763 | Double location | 160 |
| | W127 | 138.9 | 81,298 | Double location | 30 |
| | W129 | 102.9 | 37,991 | Advancing side | -110 |
| | W128 | 102.9 | 67,970 | Advancing side | 1 |
| | W115 | 102.9 | 697,953 | Advancing side | 89 |
| | W114 | 92.6 | 463,257 | Advancing side | -95 |
| | W121 | 92.6 | 476,829 | Not determined | |
| | W116 | 92.6 | 2,000,000 | Run out | |
| | W125 | 82.4 | 2,000,000 | Run out | |
| R = -1 | W122 | 82.3 | 96,400 | Advancing side | 20 |
| | W123 | 77.2 | 2,000,000 | Run out | |
| | W124 | 61.7 | 466,154 | Double location | -40 |
| | W130 | 56.6 | 222,671 | Middle | -75 |
| | W117 | 56.6 | 709,775 | Not separated | 0 |
| | W120 | 56.6 | 1,167,540 | Not separated | 0 |
| | W113 | 56.6 | 2,000,000 | Run out | |
| | W118 | 51.5 | 1,247,627 | Middle | -45 |
| | W112 | 51.5 | 2,000,000 | Run out | |

Table 6 Crack initiation location in the torsional fatigue specimens, defined in terms of the position in the weld zone.

| Load ratio | Specimen | τ_a (MPa) | Cyclic Life | Crack initiation |
|---------------|----------|----------------|-------------|------------------------------------|
| R = 0 | T17 | 100 | 8,764 | Retreating side |
| | T18 | 100 | 24,610 | Retreating side |
| | T23 | 91.6 | 208,575 | Multiple sites on retreating side |
| | T24 | 91.6 | 275,002 | Not determined |
| | T13 | 83.3 | 318,930 | Multiple sites on retreating side |
| | T14 | 83.3 | 347,127 | Not determined |
| | T15 | 75 | 427,865 | Not determined |
| | T19 | 75 | 522,030 | Two sites on retreating side |
| | T16 | 66.6 | 1,071,840 | Multiple sites on retreating side |
| | T20 | 66.6 | 2,000,000 | Not determined |
| R = -1 | T11 | 133.2 | 2,053 | Retreating side |
| | T22 | 133.2 | 652 | Advancing side |
| | T12 | 116.6 | 31,589 | Advancing side |
| | T21 | 116.6 | 11,941 | Advancing side |
| | T1 | 111.6 | 1,430 | Not determined |
| | T8 | 100 | 275,020 | Not determined |
| | T9 | 100 | 155,896 | Advancing side |
| | T10 | 100 | 917,913 | Advancing side |
| | T2 | 83.4 | 56,326 | Advancing side |
| | T6 | 83.4 | 1,726,450 | Stop-start position longitudinally |
| | T7 | 83.4 | 601,946 | Advancing side |
| | T4 | 75 | 1,304,324 | Advancing side |
| | T5 | 75 | 1,664,764 | Advancing side |
| | T3 | 66.6 | 2,000,000 | Not determined |

Table 7 Crack initiation location in the tension-torsional fatigue specimens, defined in terms of the position in the weld zone.

| Specimen | σ_a (MPa) | τ_a (MPa) | R | Θ° | λ | Cyclic Life | Crack Initiation |
|----------|------------------|----------------|----|----------------|-----------|-------------|-------------------------|
| IPh-1 | 47.4 | 27.4 | -1 | 0 | 1.73 | 47,641 | Advancing side |
| IPh-2 | 47.4 | 27.4 | -1 | 0 | 1.73 | 139,861 | Advancing side |
| IPh-3 | 39.5 | 22.8 | -1 | 0 | 1.73 | 171,506 | Retreating side |
| IPh-4 | 39.5 | 22.8 | -1 | 0 | 1.73 | 369,237 | Advancing to Retreating |
| IPh-5 | 33 | 19 | -1 | 0 | 1.73 | 355,728 | Not determined |
| IPh-6 | 33 | 19 | -1 | 0 | 1.73 | 932,288 | Retreating side |
| IPh-7 | 33 | 19 | -1 | 0 | 1.73 | 513,782 | Not determined |
| IPh-8 | 33 | 19 | -1 | 0 | 1.73 | 623,187 | Stop-start |
| IPh-9 | 39.5 | 39.5 | -1 | 0 | 1 | 160,391 | Retreating side |
| IPh-10 | 39.5 | 39.5 | -1 | 0 | 1 | 47,967 | Advancing side |
| IPh-11 | 34.3 | 34.3 | -1 | 0 | 1 | 358,240 | Not determined |
| IPh-12 | 34.3 | 34.3 | -1 | 0 | 1 | 533,508 | Advancing side |
| IPh-13 | 30.3 | 30.3 | -1 | 0 | 1 | 592,342 | Not determined |
| IPh-14 | 30.3 | 30.3 | -1 | 0 | 1 | 650,684 | Advancing side |
| IPh-15 | 30.3 | 27.4 | -1 | 0 | 1.17 | 148,831 | Retreating side |
| IPh-23 | 39.5 | 22.8251 | -1 | 90 | 1.73 | 173,954 | Retreating side |
| IPh-24 | 32.9 | 19 | -1 | 90 | 1.73 | 2,000,000 | Not determined |
| IPh-25 | 33 | 19 | -1 | 90 | 1.73 | 139,484 | Retreating side |
| IPh-26 | 39.5 | 22.8 | -1 | 90 | 1.73 | 44,499 | Weld zone |

| | | | | | | | |
|---------|---------|------|----|----|------|-----------|-------------------------|
| IPh-27 | 33 | 19 | -1 | 90 | 1.73 | 46,086 | Weld zone |
| IPh-28 | 33 | 19 | -1 | 90 | 1.73 | 857,580 | Not determined |
| IPh-29 | 35.6 | 20.5 | -1 | 90 | 1.73 | 686,557 | Advancing side |
| IPh-30 | 30.3 | 30.3 | 0 | 0 | 1 | 236,518 | Advancing to Retreating |
| IPh-31 | 25 | 25 | 0 | 0 | 1 | 175,164 | Advancing to Retreating |
| IPh-32 | 25 | 25 | 0 | 0 | 1 | 170,009 | Retreating side |
| IPh-33 | 21 | 21 | 0 | 0 | 1 | 273,482 | Retreating side |
| IPh-34 | 18.5 | 18.5 | 0 | 0 | 1 | 857,370 | Retreating side |
| IPh-35 | 18.5 | 18.5 | 0 | 0 | 1 | 548,537 | Weld zone |
| IPh-36 | 15.8 | 15.8 | 0 | 0 | 1 | 1,351,096 | Not determined |
| IPh-16 | 33 | 19 | 0 | 0 | 1.73 | 205,952 | Retreating side |
| IPh-17 | 30.3 | 17 | 0 | 0 | 1.73 | 118,631 | Retreating side |
| IPh-18 | 18.5 | 10.6 | 0 | 0 | 1.73 | 2,000,000 | Not determined |
| IPh-19 | 47.4499 | 27.4 | 0 | 0 | 1.73 | 25,614 | Retreating side |
| IPh-20 | 23.7 | 13.7 | 0 | 0 | 1.73 | 501,988 | Advancing to Retreating |
| IPh-21 | 21 | 12.2 | 0 | 0 | 1.73 | 891,341 | Advancing to Retreating |
| IPh-22 | 23.7 | 13.7 | 0 | 0 | 1.73 | 2,000,000 | Not determined |
| OoPh-37 | 33.0 | 19.0 | 0 | 90 | 1.73 | 98,938 | Retreating side |
| OoPh-38 | 29.0 | 16.7 | 0 | 90 | 1.73 | 224,230 | Retreating side |
| OoPh-39 | 23.7 | 13.7 | 0 | 90 | 1.73 | 2,000,000 | Not determined |
| OoPh-40 | 33.0 | 19.0 | 0 | 90 | 1.73 | 38,084 | Advancing side |
| OoPh-41 | 29.0 | 16.7 | 0 | 90 | 1.73 | 121,400 | Advancing side |

| | | | | | | | |
|---------|------|------|---|----|------|-----------|-----------------|
| OoPh-42 | 23.7 | 13.7 | 0 | 90 | 1.73 | 2,000,000 | Not determined |
| OoPh-43 | 26.4 | 15.2 | 0 | 90 | 1.73 | 745,539 | Advancing side |
| OoPh-44 | 29.0 | 29.0 | 0 | 90 | 1.00 | 34,544 | Retreating side |
| OoPh-45 | 21.1 | 21.1 | 0 | 90 | 1.00 | 2,000,000 | Not determined |
| OoPh-46 | 26.4 | 26.4 | 0 | 90 | 1.00 | 80,612 | Not determined |
| OoPh-47 | 25.0 | 25.0 | 0 | 90 | 1.00 | 945,586 | Not determined |

Table 8 Summary of the crack location information for all specimens, in terms of initiating at either the advancing or retreating side of the weld.

| | Tensile | Torsion | In Phase | Out Of Phase | Sum |
|------------------------|----------------|----------------|-----------------|---------------------|------------|
| Advancing side | 8 | 9 | 11 | 3 | 31 |
| Retreating side | 2 | 7 | 12 | 3 | 24 |
| Other | 2 | 1 | 4 | 0 | 7 |
| Not determined | 6 | 7 | 9 | 5 | 27 |



Figure 1 Illustration of a tube specimen in position ready to be welded.

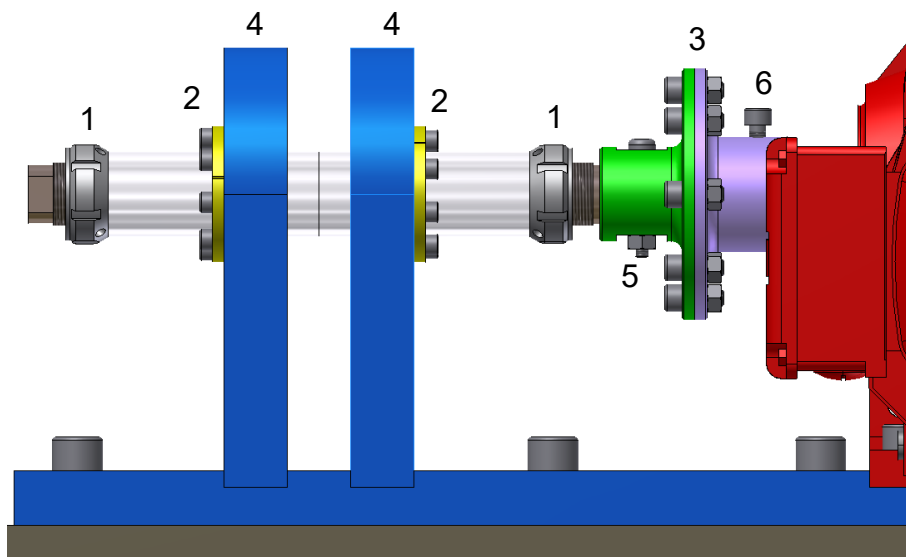


Figure 2 Schematic diagram showing the various components in the tube clamping system.

Weld Sequence

1. Pin moves toward weld centreline
2. Pin touches tube for zero reference of plunge depth
3. Start spindle rotation
4. Plunge pin and shoulder
5. Ensure shoulder in contact with pipe
6. Initiate pipe rotation
7. Rotate pipe 720° to achieve good surface finish (2 full revolutions)
8. Initiate pin retraction after 630° rotation keeping pipe rotating to eliminate exit hole
9. Retract shoulder

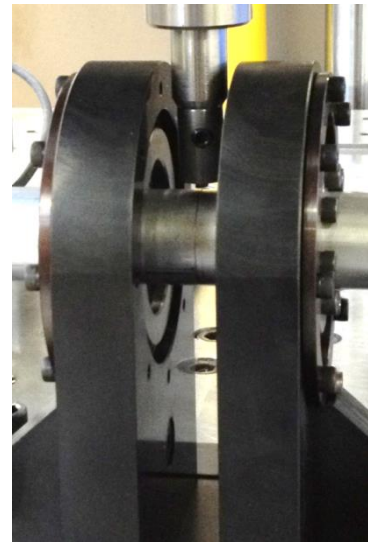


Figure 3 Sequence of events required in making a sound FS weld in the 6082-T6 aluminium tubes.



Figure 4 Influence of the weld process parameters of plunge depth, rotational feed rate and tool rotational speed on the quality of weld surface finish.

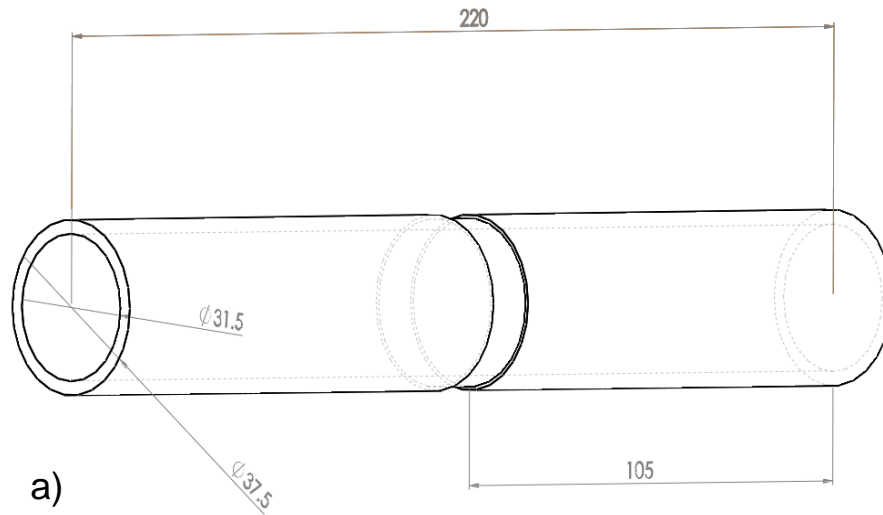


Figure 5

a) Approximate dimensions of the tubular fatigue specimens. b) Image showing a



b)
typical welded specimen.

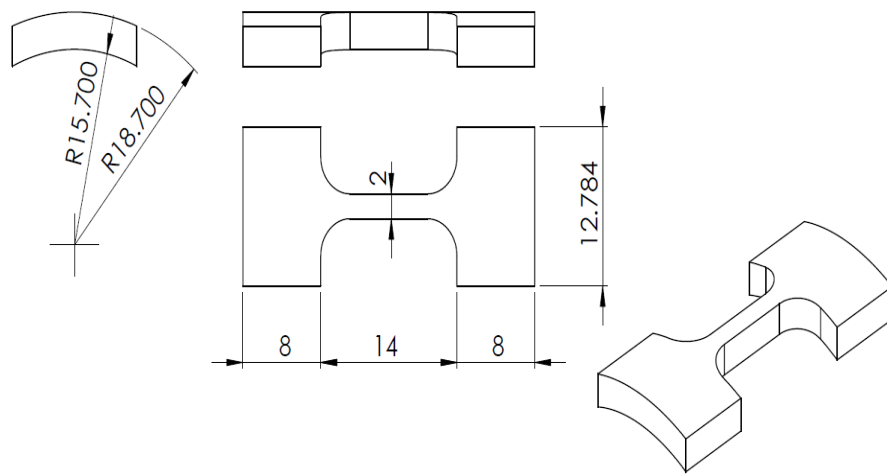


Figure 6 Microtensile specimen geometry; the curved surface requires support during clamping and testing.

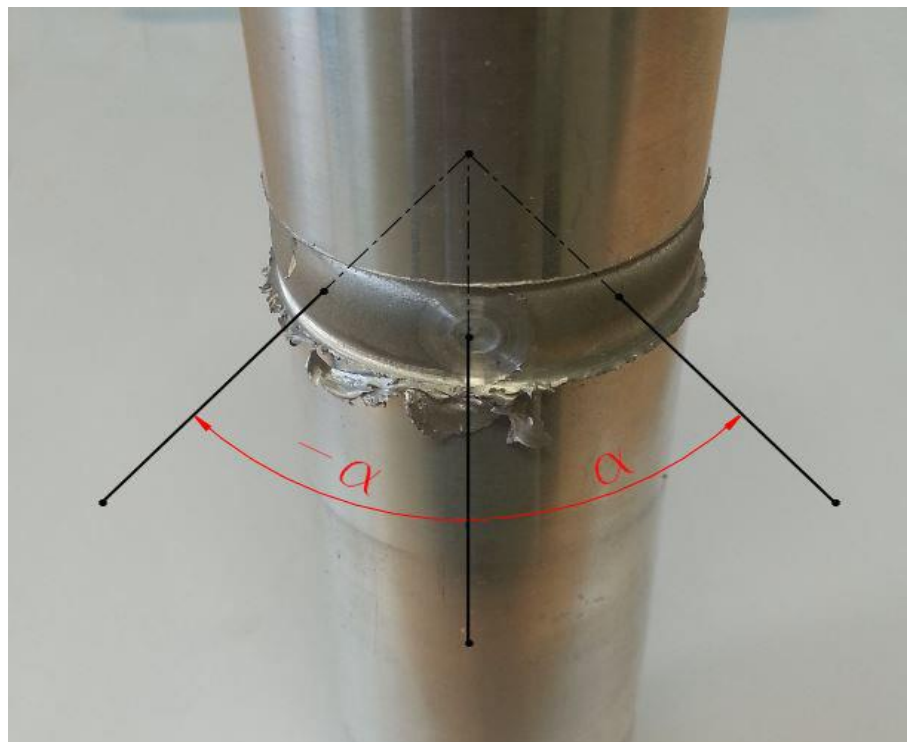


Figure 7 Coordinate system used to define the crack initiation sites.

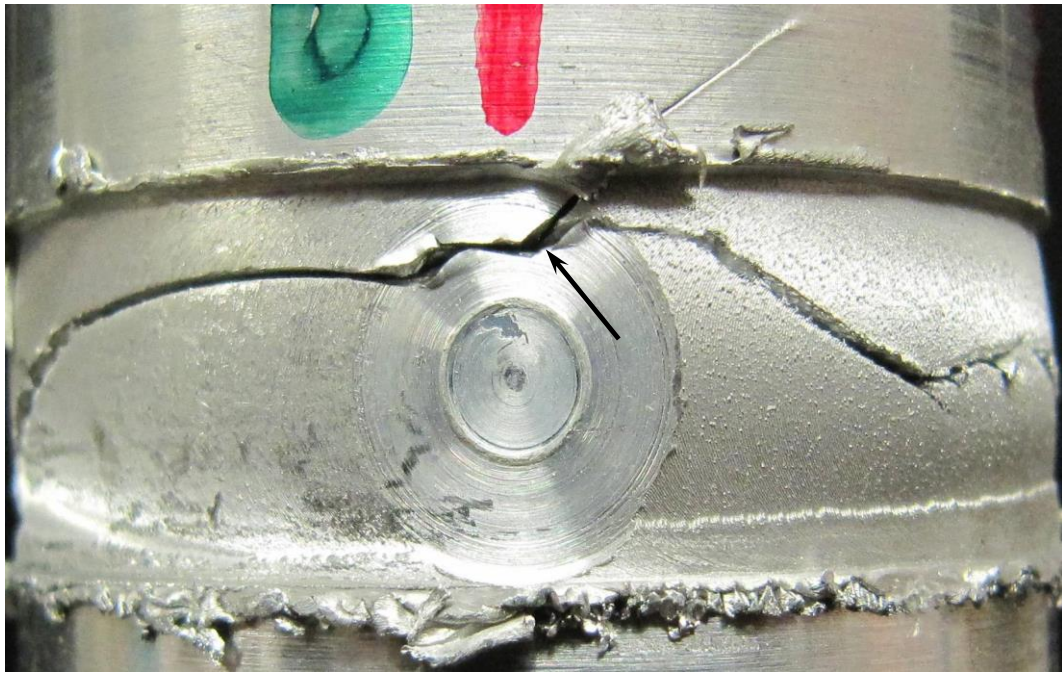


Figure 8a Crack initiation site (marked with arrow) in specimen T4 tested in torsion at $R = -1$ with a shear stress amplitude of 75 MPa.



Figure 8b Crack initiation site in specimen T22 tested in torsion at $R = -1$ with a shear stress amplitude of 133 MPa. The crack runs around the undercut groove on the advancing side of the weld. This is the most common mode of failure in both tension and torsion fatigue specimens.



Figure 9 In-phase tension-torsion fatigue test (IPh21) showing that the crack has initiated along the tool shoulder groove on the retreating side and then moved across to the advancing side of the weld.

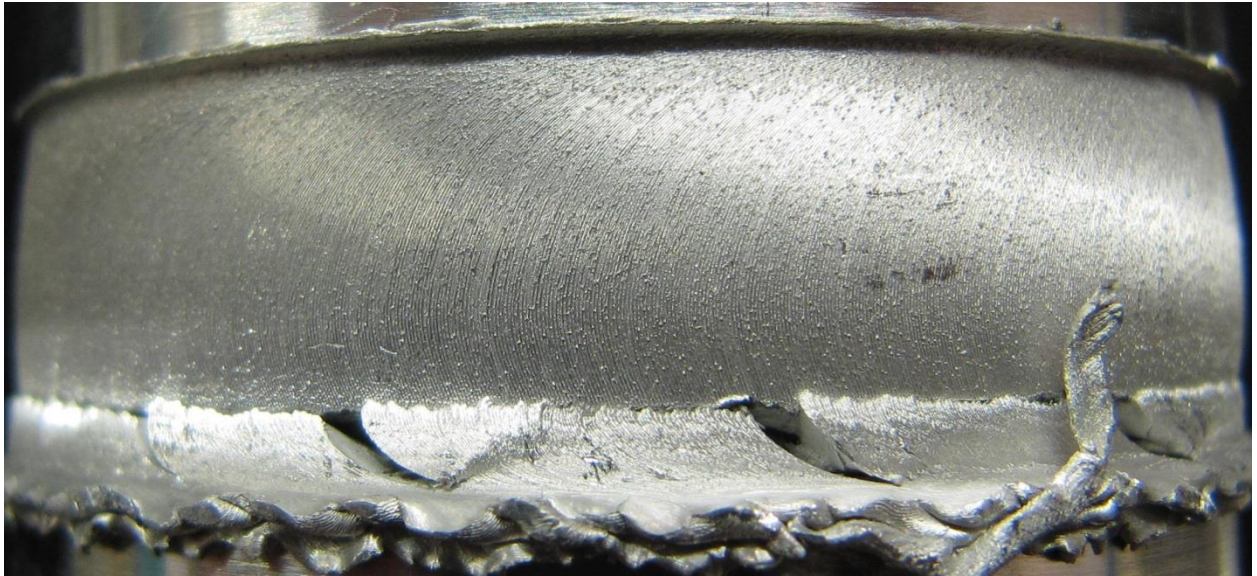


Figure 10 Multiple crack initiation sites observed in torsion fatigue at $R = 0$. This image shows specimen T23.

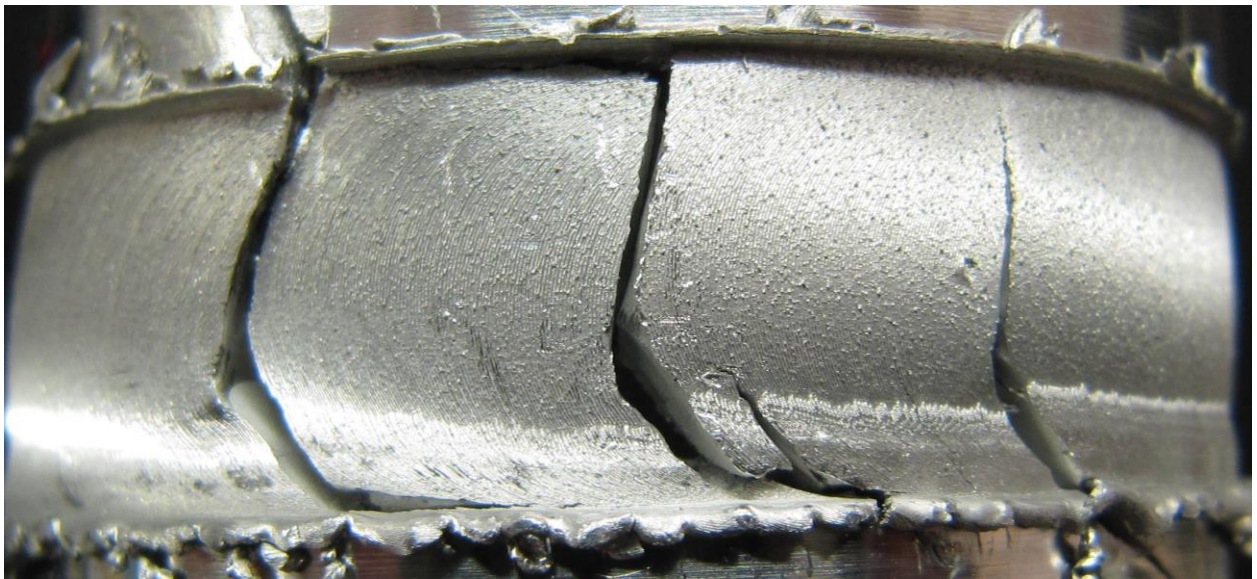


Figure 11 Multiple crack initiation appears to be exacerbated at lower torsional stress and hence longer fatigue lives. This image shows specimen T16.

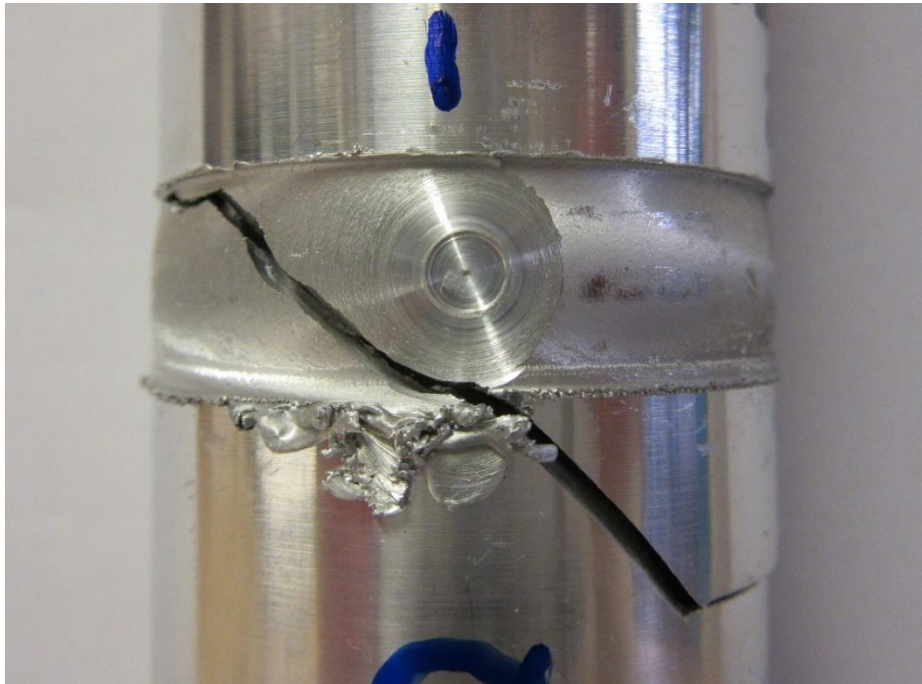


Figure 12 Certain tension-torsion specimens showed crack initiation associated with the stop-start position. This is specimen IPh8.

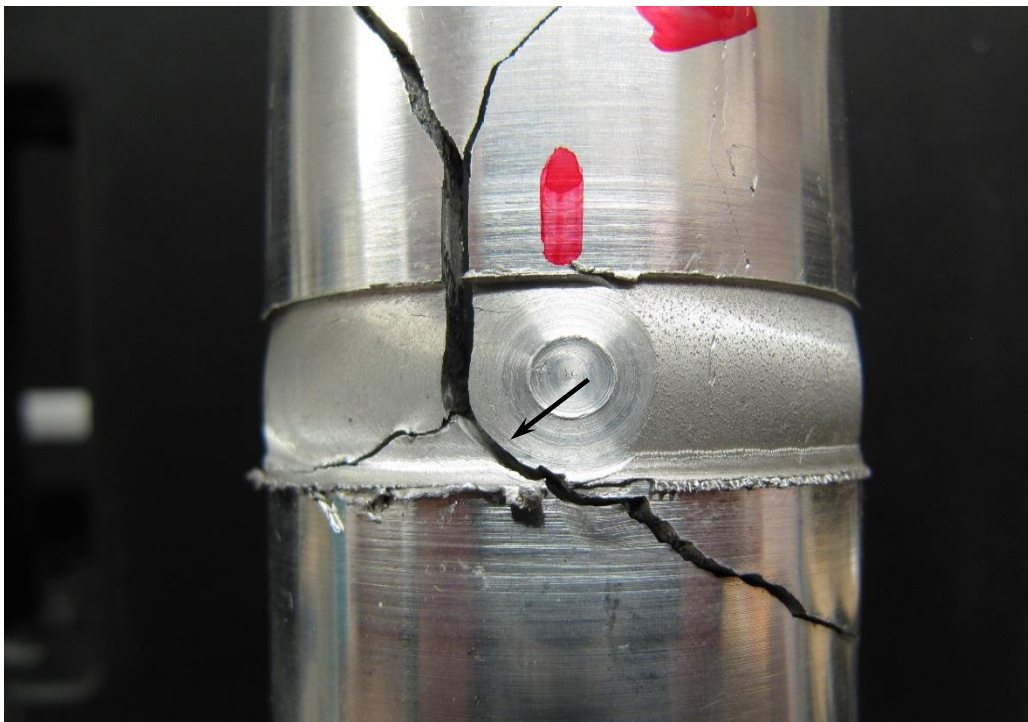


Figure 13 Specimen T6 which showed classic shear crack bifurcation. The arrow marks the crack initiation site which is also associated with the stop-start position.

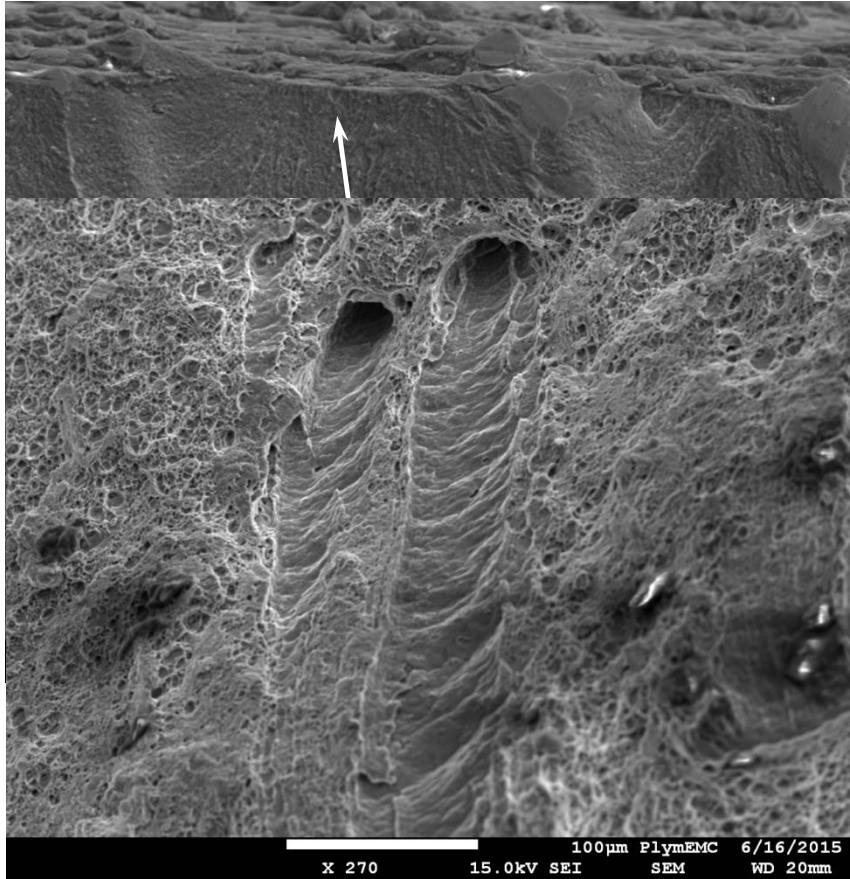


Figure 14 SEM fractograph showing crack initiation (arrow) between surface tool marks in tensile fatigue specimen W121. The small white bar at the bottom of the picture is a 10 µm marker.

Figure 15 Wormhole defects on the fast fracture region of tensile fatigue specimen W117. As expected the fracture mechanism is microvoid coalescence.

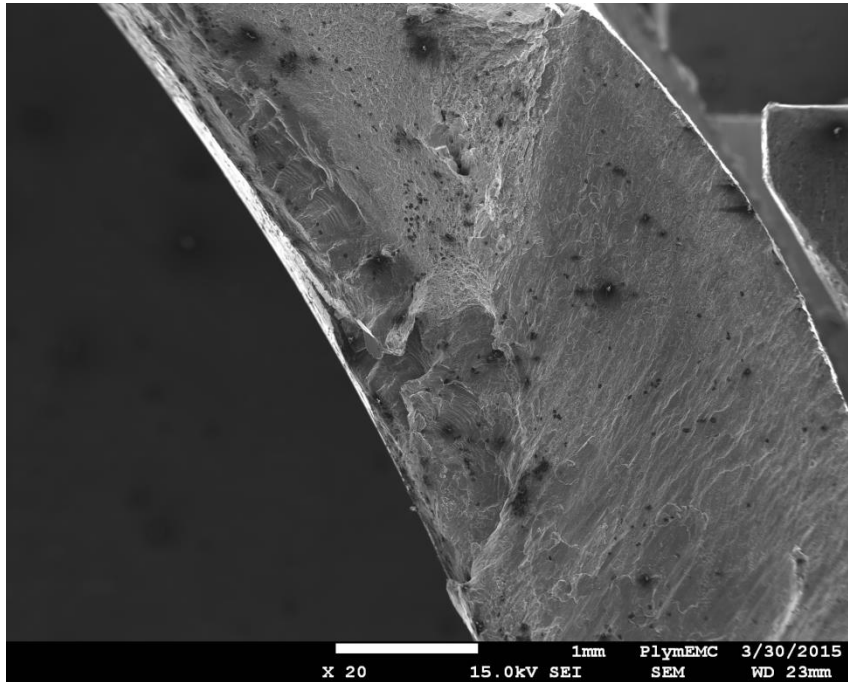


Figure 16 Clear evidence of initiation of the primary fatigue crack from the outer edge of specimen IPh2 can be seen at the upper right hand corner in this image.

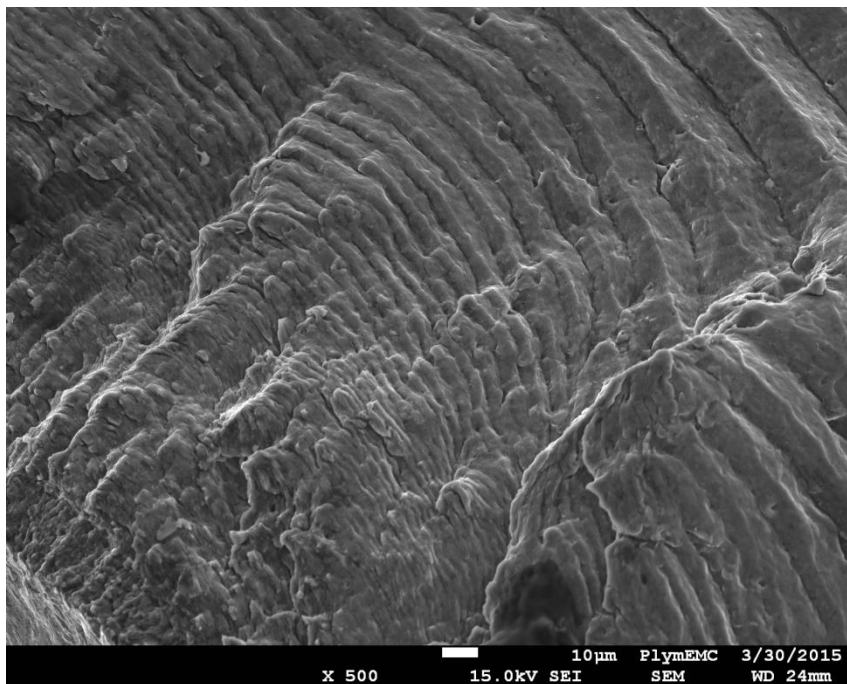


Figure 17 A smaller secondary site of fatigue crack initiation is present at the inner edge of tube specimen IPh2 in the lower left corner of this image.

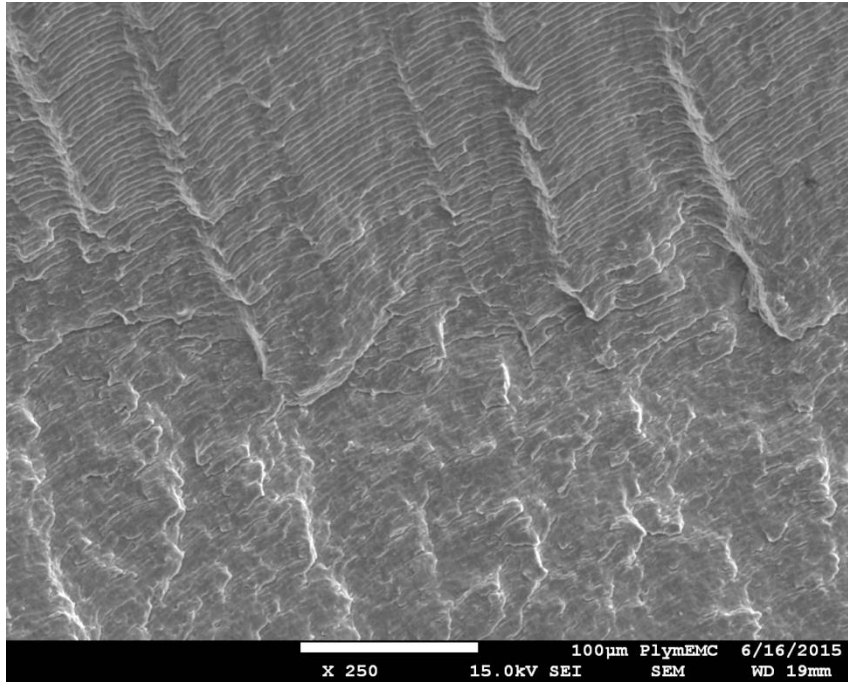


Figure 18 The mechanism of fatigue crack growth was by ductile striation formation; this image shows the fracture surface on tensile fatigue specimen W130 and the crack growth direction is from the bottom of the image to the top.

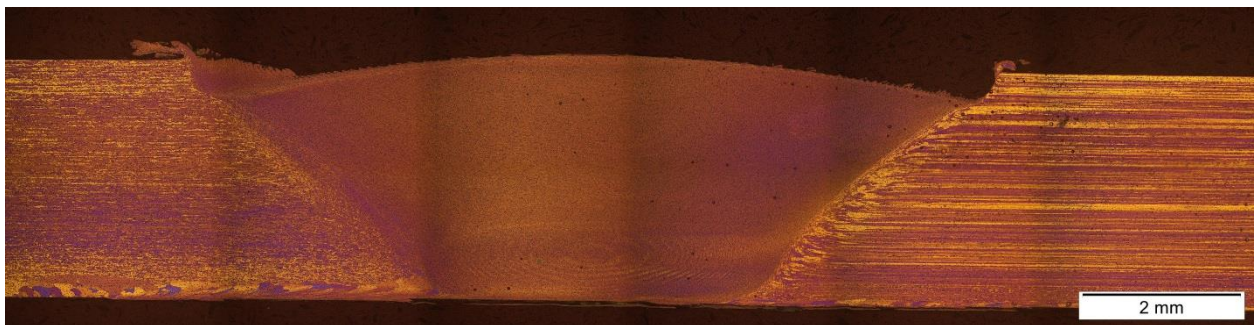


Figure 19 Polarised light metallographic montage showing the complete weld zone in specimen T6 tested in torsional fatigue.

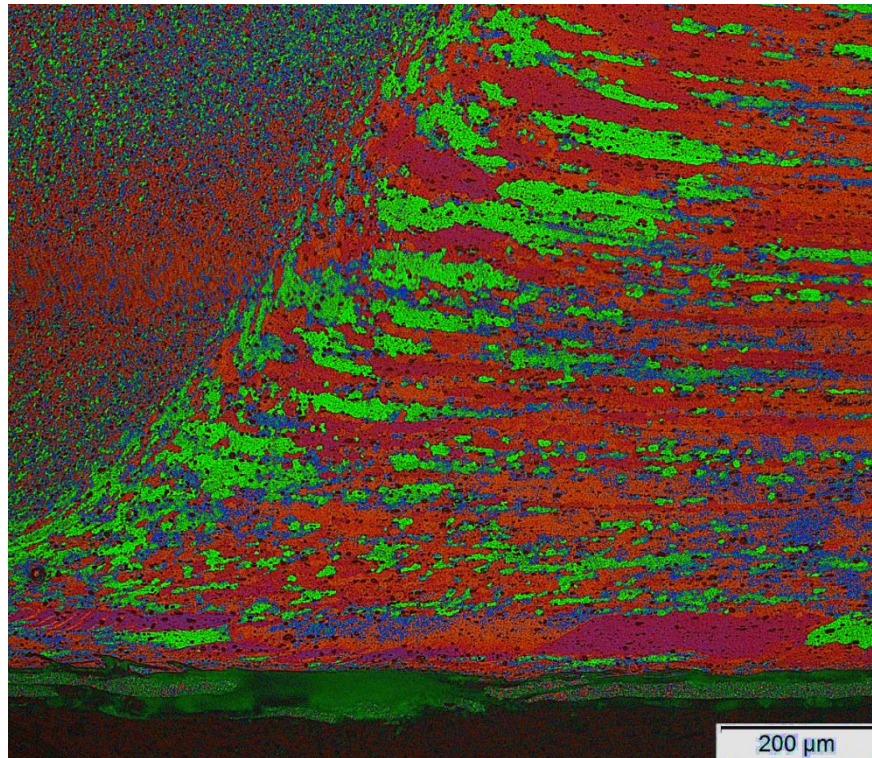


Figure 20 Polarised light micrograph showing the edge of the weld at 100x magnification.

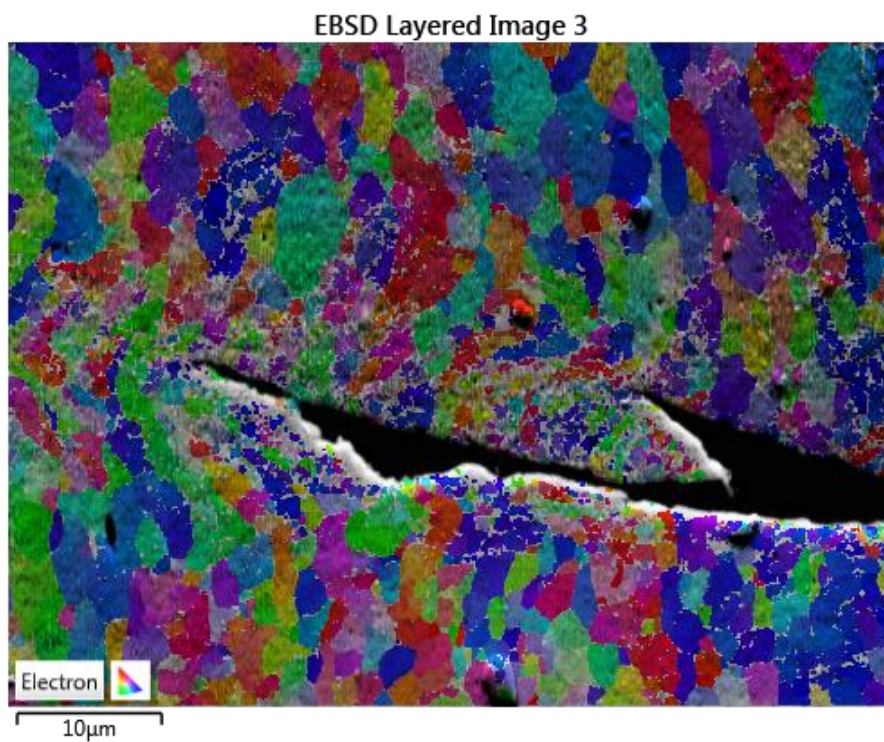


Figure 21 EBSD image showing the crack tip region in specimen T6 at 2,000x magnification.

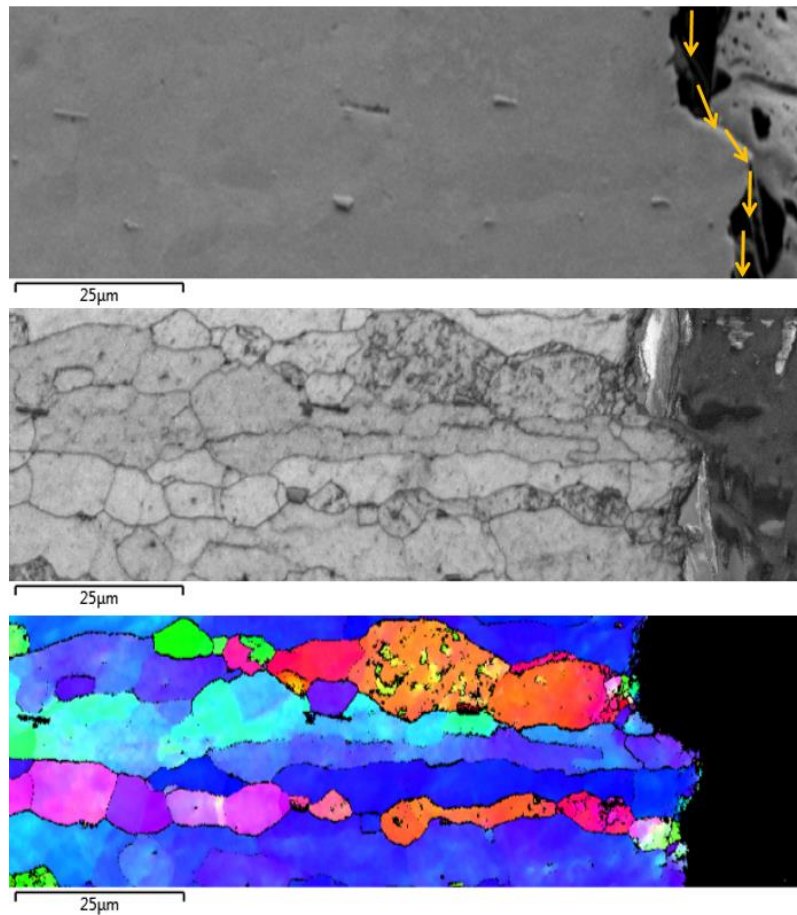


Figure 22 EBSD images of crack growth through the thickness of the tube wall. This shows is the heat-affected zone on the parent plate side of the crack and the crack growth direction is indicated in the top image.
